Investigation of Frequency Selective Surfaces for a THz Gyro-Multiplier Output System

Xiang Li, Xiaoming Liu, Kevin Ronald, Wenlong He, Yang Zeng, Yasir Alfadhl, Robert Donnan, Adrian Cross, Xiaodong Chen

***Abstract*—The recent development of some high-power THz vacuum electronic devices calls for the application of space filters such as frequency selective surfaces (FSSs) and polarization dividers. This paper presents the comparative study of two types of FSSs for a THz gyro-multiplier output system, one with high-pass characteristic while the other one with low-pass functionality. Both FSSs are designed, fabricated and experimentally tested between 200 and 1600 GHz to verify their capability of separating the dual-frequency output from the gyro-multiplier. The high-power operation capability of the FSSs is also characterized by taking both the corona discharge and volumetric breakdown into consideration at the frequencies of interest. Based on the comparative study of the performance, the fabrication challenge and the high-power capability between the two FSSs, a generalized conclusion is given regarding the choice of the FSSs for high-power THz application.**

***Index Terms*—Frequency selective surface, Gyro-multiplier, Output systems, High-power breakdown.**

I. Introduction

In recent years, the application of the space filters such as the frequency selective surfaces (FSSs) [1] and polarization dividers [2] in high-power vacuum electronic devices (VEDs) has drawn considerable attention. In Institute of Applied Physics (IAP), Russia, a polarization divider is adopted in a gyrotron traveling wave tube to simplify the input/output system of the device [3]-[5]. Since 2011, extensive investigations have been carried out on the high-power susceptibility of the miniaturized FSS using the magnetrons in University of Wisconsin, United States [6]-[9]. In 2015, the combination of quasi-optical mode converters (QMCs) [10]-[12] and FSSs in the output systems of the double-beam gyrotron and the fourth-harmonic gyro-multiplier [13] has been proposed in [14] and [15], respectively. Further development of the two systems are reported in [16] and [17], respectively. In these systems, the QMCs are used to transform the high-order waveguide modes into quasi-Gaussian beams and the FSSs are used to spatially separate the converted beams according to the frequencies. Compared with the traditional waveguide transmitters and filters, the designed systems bring more compactness and lower ohmic losses. Since such kind of output system is anticipated to be applicable to the gyro-devices with simultaneous multi-frequency outputs, a detailed study of the candidate FSSs is indispensable. Also, it is reasonable to consider using the FSSs in other VEDs with simultaneous multi-frequency generation. When being integrated in the high-power THz VEDs, not only the transmission and reflection performance, but also the fabrication and high-power operation challenge of the FSSs should be considered.

In this paper, we are dedicated to conduct a comparative study between two candidates, namely a high-pass and a low-pass FSS, both of which are based on the configuration of periodic perforations on the metal plates. Although this type of FSS has been reported [18]-[21], we focus on their potential to be integrated within the output system of the high-power gyro-multiplier and operation with oblique incident wave in THz band. Besides, we also consider in this paper using such configuration as a low-pass filter, which is rarely reported in literature. To do so, we comparatively present the design, fabrication, surface finishing characterization and experimental verification of both FSSs. Then, based on the tested surface finishing condition of the fabricated FSSs and numerical simulation, we demonstrate the high power handling capability of both FSSs by considering the corona discharge [22] as well as the volumetric breakdown [23]. Finally, a systematic comparison between the two FSSs regarding the separation capability, the fabrication challenge and the power-handling capability is carried out. Based on the comparison, the conclusion is made about the choice of the proper FSS configurations for some other high-power VEDs with simultaneous multi-frequency outputs.

The remaining part of this paper is organized as follows: Section II presents the overview of the quasi-optical output system and the configuration of FSSs that can be applied. Section III focuses on the design, fabrication and experimental test of both the high-pass and low-pass FSS. Section IV assesses the high-power breakdown susceptibility of the two FSSs. Section V describes a detailed comparison between the two configurations. Section VI concludes this paper.

Manuscript received in 2016. This work was supported in part by the National Nature Science Foundation of China under the contract number of 61401031 and the Scientific Research Foundation for the Returned Overseas Chinese Scholars, State Education Ministry. (Corresponding Author: Xiaoming Liu.)

Xiang Li, Yang Zeng, Yasir Alfadhl, Robert Donnan and Xiaodong Chen are with the School of Electronic Engineering and Computer Science, Queen Mary University of London, London, E1 4NS, UK (e-mail: xiang.x.li@qmul.ac.uk).

Xiaoming Liu is with the School of Electronic Engineering, Beijing University of Posts and Telecommunications, Beijing 100876, China (e-mail: xiaoming_liu@bupt.edu.cn).

Kevin Ronald, Wenlong He and Adrian Cross are with the Department of Physics, Scottish Universities Physics Alliance (SUPA), University of Strathclyde, Glasgow G4 0NG, UK (e-mail: a.w.cross@strath.ac.uk).

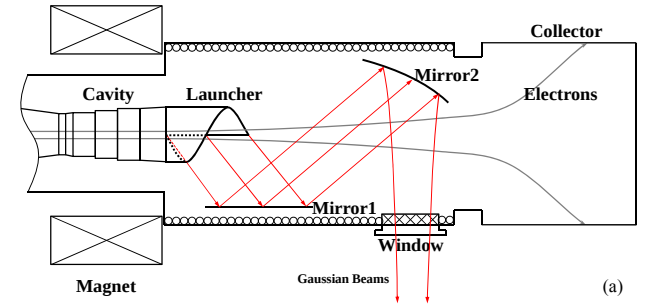

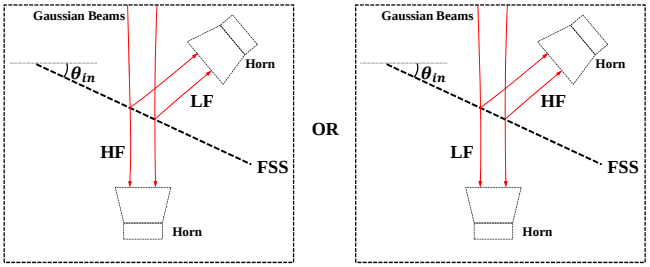

Fig. 1. An overview of the designed output system for the gyro-multiplier. (a) The generation of the two Gaussian beams; (b) The separation of the two beams with a high-pass FSS; (c) The separation with a low-pass one.

TABLE I
CONTENTS OF THE CONVERTED QUASI-GAUSSIAN BEAMS FROM THE FOURTH-HARMONIC GYRO-MULTIPLIER. f AND P ARE THE FREQUENCY AND THE POWER, RESPECTIVELY.

	LF	HF
f (GHz)	342	1368
P (kW)	1.628	0.109

II. SYSTEM CONFIGURATIONS

The application of the designed FSSs is shown in Fig. 1. The gyro-multiplier is a high-power vacuum electronic source that combines the conventional electron cyclotron maser and frequency multiplication technique [24]. In the fourth-harmonic gyro-multiplier with sectioned cavity [13], a high-frequency (HF) radiation at the fourth electron cyclotron harmonic is generated from the nonlinear interaction between the gyrating electron beam and the self-excited low-frequency (LF) wave at the fundamental harmonic. As a result, two high-order cylindrical waveguide modes, one at 342 GHz and the other one at 1368 GHz, are simultaneously generated from the cavity. The modes are then transformed into two quasi-Gaussian beams by a dual-frequency quasi-optical mode converter (DQMC) consisting a launcher and two mirrors, before being transmitted through the window, as shown in Fig. 1. The contents of the transmitted quasi-Gaussian beams can be summarized in TABLE I. The designed FSSs in our case are placed at the shared waist position of the HF and LF beams to separate them in space. The cases where the FSSs are not placed at the beam waists are discussed in detail in [25], along with advanced numerical techniques. To avoid the reflection

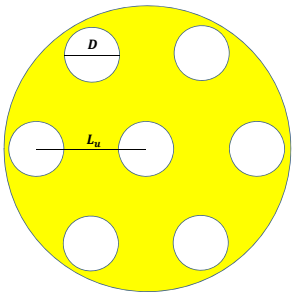

Fig. 2. A regional view of a FSS composed of hexagonal array of circular perforations.

back into the DQMC and the beam-wave interaction cavity, the FSSs are designed for oblique incidence with an incident angle of $\theta_{in} = 15°$. The incident quasi-Gaussian beams have a linear polarization pointing outwards from the paper [17], thus form a TE mode incidence regarding the FSSs. In Fig. 1, the directions of the rays after passing through the FSSs, which follow that of the incident beam, are drawn without considering the possible grating lobes. For high-power THz application, all-metal FSSs are promising for good heat dissipation capability and potential to avoid fabricating as well as aligning very fine structures on dielectric substrates.

In our previous work [17], a high-pass FSS based on a square array of periodic perforations on a brass plate is reported with tested insertion loss values of 32.7 and 2.8 dB at 342 and 1368 GHz, respectively. The configuration is shown as Fig. 1 (b). While showing good reflectivity of the LF content, the transmission coefficient of the HF content is low, due to the diffraction into the first grating lobe and limited fabrication precision. To reduce the diffraction loss, it is suggested that the inter-element spacing should be reduced from 190 to 180 μm. However, this is challenging due to the limitation of the chemical etching technique [26]. In fact, some undesired inter-connection between neighboring holes has already been detected for the inter-element spacing of 190 μm.

Thus, a high-pass FSS with hexagonal array of circular perforation is adopted in this work, as shown in Fig. 2. It is designed to be resonantly transparent at 1368 GHz while opaque at 342 GHz. For a hexagonal array, the distance L_u between individual perforation and its neighboring holes are constant. Within the diffraction limit of the wave at 1368 GHz, the maximum inter-element spacing allowed by the hexagonal array is about 15% larger than that by the square one [27]. Such feature enables the increase of L_u from 190 to 200 μm, which alleviates the fabrication challenges without causing the diffraction problem. In Fig. 2, the diameter of the circular perforations is D. The thickness of the metal plate is H.

Another method to alleviate the fabrication challenge is using a low-pass FSS in the system, as shown in Fig. 1 (c). Considering the advantage of the hexagonal array, the low-pass FSS has the same layout as the high-pass one in Fig. 2, but is designed to be resonantly transparent at 342 GHz while reflective at 1368 GHz. By doing so, the L_u, D and H values of the low-pass FSS are nearly four times larger than those of the high-pass one, allowing much more flexibility in fabrication. As most of the previous research on the all-metal FSS formed

TABLE II
DESIGNED AND AVERAGED FABRICATED SIZES OF THE TWO FSSS.

	L_u (μm)	D (μm)	H (μm)
High-pass Designed	200	140	100
High-pass Fabricated	199	142	100
Low-pass Designed	750	560	400
Low-pass Fabricated	751	562	400

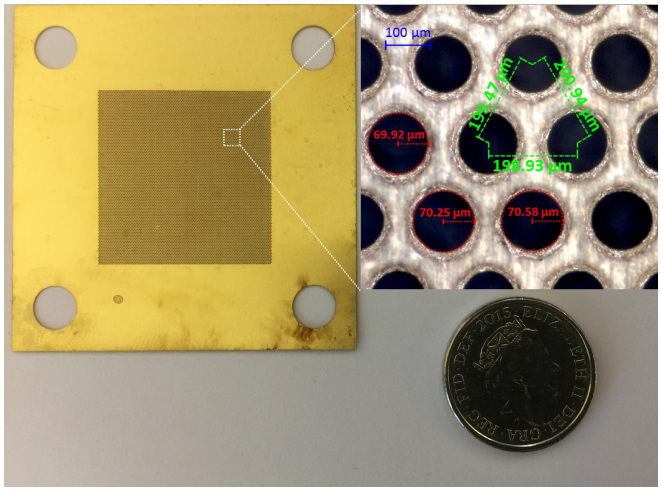

(a)

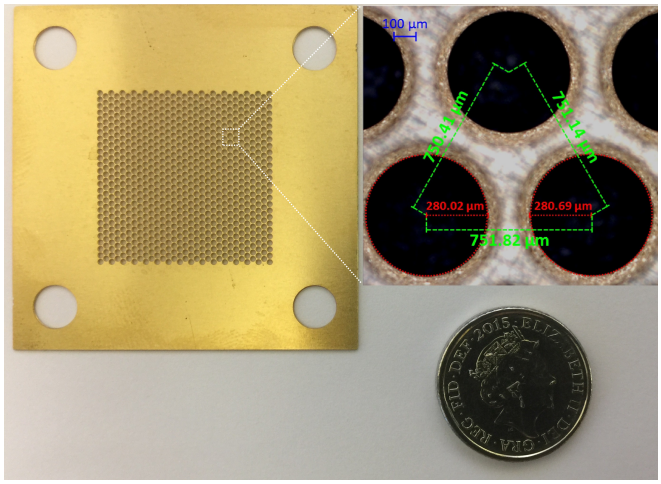

(b)

Fig. 3. The fabricated FSSs and the corresponding microscopic view the elements. (a) The high-pass one; (b) The low-pass one.

by periodic perforations focuses on the high-pass scheme, to employ it as a low-pass filter is a unique perspective worth looking into.

III. DESIGN, FABRICATION AND TEST OF THE FSSS

Knowing the required pass bands, the initial design of the FSSs can be obtained in the fashion as described in [19]. The designed parameters are then optimized in CST Microwave Studio (MWS) [28] to ensure satisfying tolerance regarding the possible fabrication error. The optimized structural parameters

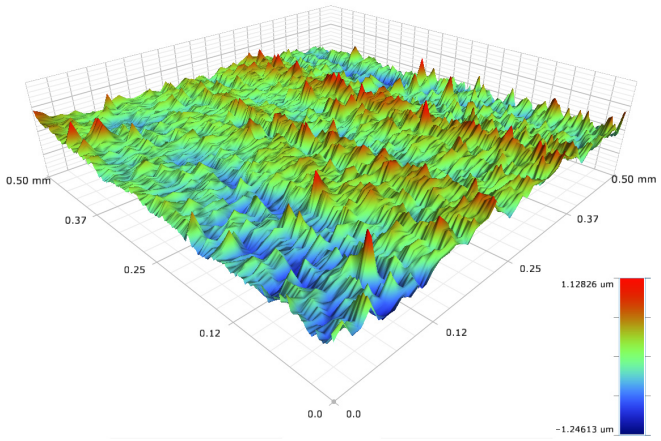

Fig. 4. The surface roughness profile of the fabricated high-pass FSS tested by the DektakXT stylus surface profiler.

of the two FSSs are listed in TABLE II.

Fig. 3 (a) shows the fabricated high-pass FSS, which is based on an array of 11600 perforations. During the process of fabricating the perforations with 140 μm diameter, the concentration of the acid solution and the exposure time must be precisely controlled to avoid excessive or inadequate etching problem. Fig. 3 (b) shows the fabricated low-pass FSS based on an array of 822 holes. Both FSSs have the same overall size of 40×40 mm^2. The material of the metal plates is brass. Before testing, the fabricated FSSs are cleaned by ultrasound. Each of the averaged fabricated sizes of the FSSs as listed in TABLE II is based on 20 sampling measurements at different locations. L_u and D are measured by a microscope while H is measured by a micrometer.

For our application within the THz frequency range, the surface condition of the FSS is essential because the surface roughness level not only determines the actual conductivity of the metal, but also affects the high-power handling capability of the periodic structure. Fig. 4 shows a typical measured surface profile of the fabricated high-pass FSS with a DektakXT stylus surface profiler [29]. According to the surface profile data, the root-mean-squared (rms) surface roughness values of the high-pass and the low-pass FSSs are estimated to be within the range of 201±15 nm, which are about half of the value for the fabricated sample in [17]. Such reduction of the surface roughness can help to increase the effective conductivity and the volumetric breakdown threshold of air at the vicinity of the metal surface. The mean surface roughness of both FSSs is calculated to be within the range of 153±10 nm.

In the simulation with CST MWS and ANSYS HFSS [30], we need to consider the influence of the surface roughness of the brass plate on its effective conductivity, σ_{eff}. According to the experimentally verified Hammerstad-Bekkadal (HB) formula [31],[32],

$$\sigma_{eff} = \sigma_i \cdot \left\{1 + \frac{2}{\pi} arctan\left[1.4 \cdot \left(\frac{s}{\delta}\right)^2\right]\right\}^{-2} \quad (1)$$

in which σ_i and δ are the conductivity and skin depth of the metal with flat surface, respectively. s represents the rms surface roughness value. Assuming σ_i value of 2.74×10^7 S/m

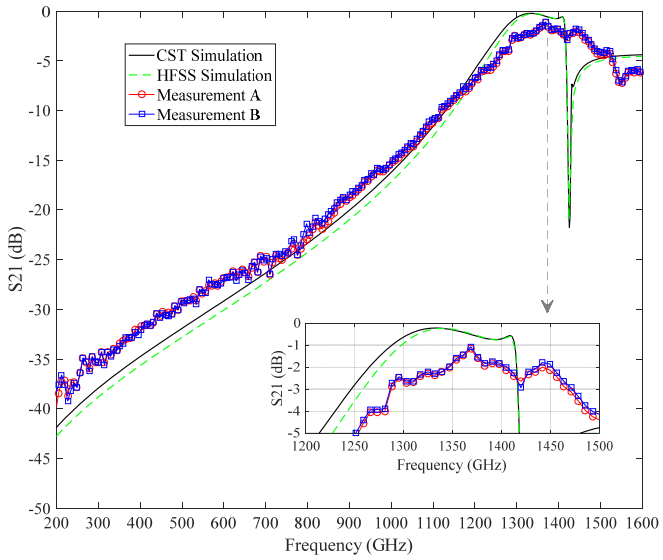

(a)

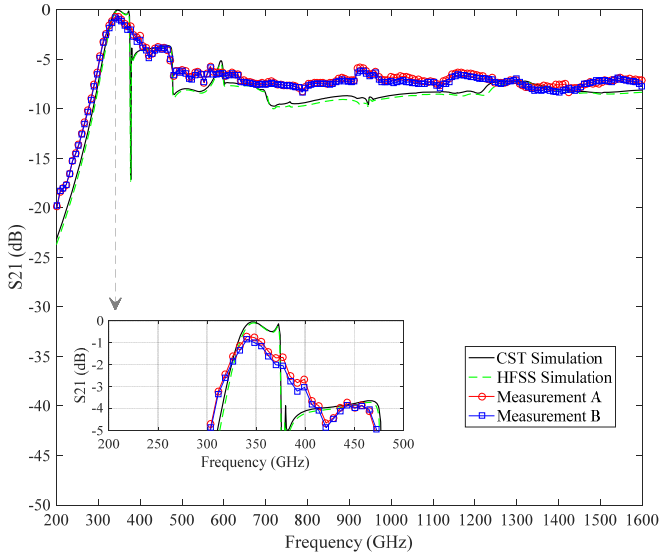

(b)

Fig. 5. Comparison of the simulated and experimentally tested S_{21} parameter variation with frequency: (a) for the high-pass FSS; (b) for the low-pass FSS. The incidence angles in all cases are fixed at 15°. The red circles and blue squares are the measured S_{21} values when the two sides of individual FSS sample are facing the incoming testing beam, respectively.

and s value of 201 nm for brass, σ_{eff} values at 342 and 1368 GHz can be estimated as 0.93×10^7 and 0.74×10^7 S/m, respectively. As the effective conductivity variation with frequency is small and has negligible impact on the simulated S_{21} performance, its value used in the simulations is chosen as 0.74×10^7 S/m. In the simulation, the periodic boundary condition is adopted on the four edges of the unit cell, hence the incident plane wave can be decomposed into a series of Floquet modes [28]. To characterize the high-pass FSS in the frequency range between 200 to 1600 GHz, a total number of 10 Floquet modes are calculated, including 4 evanescent modes and all of the 6 propagating modes, which is sufficient to take into consideration of the wave diffraction on the periodic surface. In the simulation of the low-pass FSS, a total number of 92

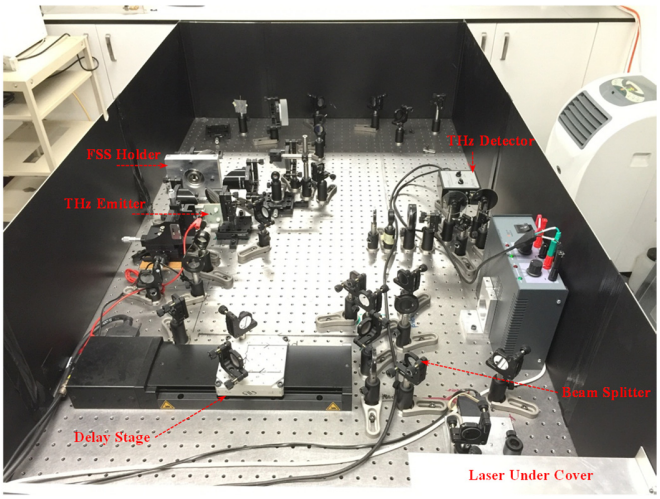

Fig. 6. The THz-TDS bench used for the experimental test of the FSSs.

Floquet modes are considered, including 4 evanescent modes and all of the 88 propagating modes in the frequency range between 200 to 1600 GHz. The fabricated sizes in TABLE II are used in the simulation, results of which are shown in Fig. 5. It can be seen that the results from both numerical tools agree well, which verifies the correctness of the modeling.

Since the testing frequency range of the commercially available vector network analyzer is typically below 1.1 THz [33], the designed FSS is characterized by a THz-TDS system [34] as shown in Fig. 6, which has a dynamic range between 0.1 and 3 THz. A femtosecond laser beam is generated from a Ti:Sapphire laser, which is then split into a pump and probe laser beam. The pump laser beam, after passing the delay stage, is used for excitation of the photoconductive antenna to generate THz radiation. The radiation is then guided by a number of mirrors to go through the sample. The transmitted THz signal can be detected by the probe laser beam by electro-optical sampling. The electric field amplitude variation of the THz radiation as a function of the time delay induced by the delay stage can be obtained. By applying the Fourier Transformation, the equivalent frequency domain spectrum can be generated. Each experimental S_{21} curve is based on the average of five tests and the error range of the tested insertion loss value at each frequency point is ±0.2 dB.

Fig. 5 shows the comparison between the simulated and the measured S_{21} curves. The results from the simulation and the experimental test reasonably agree with each other. A number of factors may cause the differences: the fabrication error of the FSSs, the finite-size effect of the fabricated FSSs, the different incident waves used in the simulation and the experimental test as well as the limited Gaussian content of the testing THz beam. In particular, one disagreement to be mentioned is that the transmission dips predicted by the numerical simulations, at about 1400 GHz for the high-pass FSS and at 400 GHz for the low-pass one, are not observed in the corresponding experiments. Such difference can be explained by two factors. On the one hand, the incident field used in the theoretical analysis is set as plane wave, while that adopted in the experiments is quasi-Gaussian beam with non-uniform field distribution and finite beam size [19]. On the other hand, in the

TABLE III
SUMMARY OF THE S_{21} PARAMETERS AT THE DESIGNED FREQUENCIES OF THE TWO FSSS.

	342 GHz	1368 GHz
High-pass Simulated (dB)	-36.98	-0.48
High-pass Tested (dB)	-34.10	-1.13
Low-pass Simulated (dB)	-0.17	-7.81
Low-pass Tested (dB)	-0.80	-7.89

simulation with the periodic boundary condition, it is assumed that the neighboring unit cells are identical, whose mutual coupling induces the transmission dips [18]. However in the experiment, the dimensions of adjacent fabricated cells may vary, which introduces different mutual coupling effects.

The simulated and experimental S_{21} values of the two FSSs at the frequencies of interests are summarized in TABLE III, where the former are derived by averaging the results from CST MWS and HFSS, and the latter are based on the average of the measurement curves of Fig. 5. Both FSSs show satisfying transmission or reflection performance at the designed frequencies. Due to the fact that the output frequency bandwidth of the gyro-multiplier is as narrow as 0.015% [13], both FSS will be effective within the whole operational range of the device. For the high-pass FSS, the coupling between the incident wave and the waveguide modes of the circular perforations is strong at 1368 GHz, which enables the resonant transmission at this frequency. At 342 GHz, the wave is rejected due to the reciprocal interaction between adjacent perforations of the periodic array as well as the very low coupling coefficient at the interface between the FSS screen and the incoming wave.

For the low-pass FSS, the periodic surface is in resonant with and transmits the wave at 342 GHz. At 1368 GHz where the wavelength is much smaller than the diameter of the perforations, the transmission property is mainly determined by the side lobes level and the porosity of the array [35]. Assuming an incident power of 109 W at 1368 GHz as listed in TABLE I, the reflected power is calculated to be 53.2 W, 22.6% of which is contained in the cross-polarized content. It is also derived from the numerical simulations that 25.4 W of power is contained in the main lobe of the reflected wave, which can be efficiently collected by a horn antenna as shown in Fig. 1 or subsequent reflectors. Such power level is still appreciable when one considers the relatively low availability of high-power sources at this frequency. The collected power can be applied in the plasma scattering measurement with high resolution [36], where radiation source of Watt's level will be sufficient at 1368 GHz.

It is known that the reflection at 342 GHz is mainly specular for the high-pass FSS, while that at 1368 GHz for the low-pass FSS is more diffusive. By incorporating the low-pass FSS as shown in Fig. 3 (b) into the original quasi-optical output system model [17] in FEKO [37], the amount of power reflected back into the DQMC is calculated to be 2.94 W, which is acceptable for the normal operation of the system.

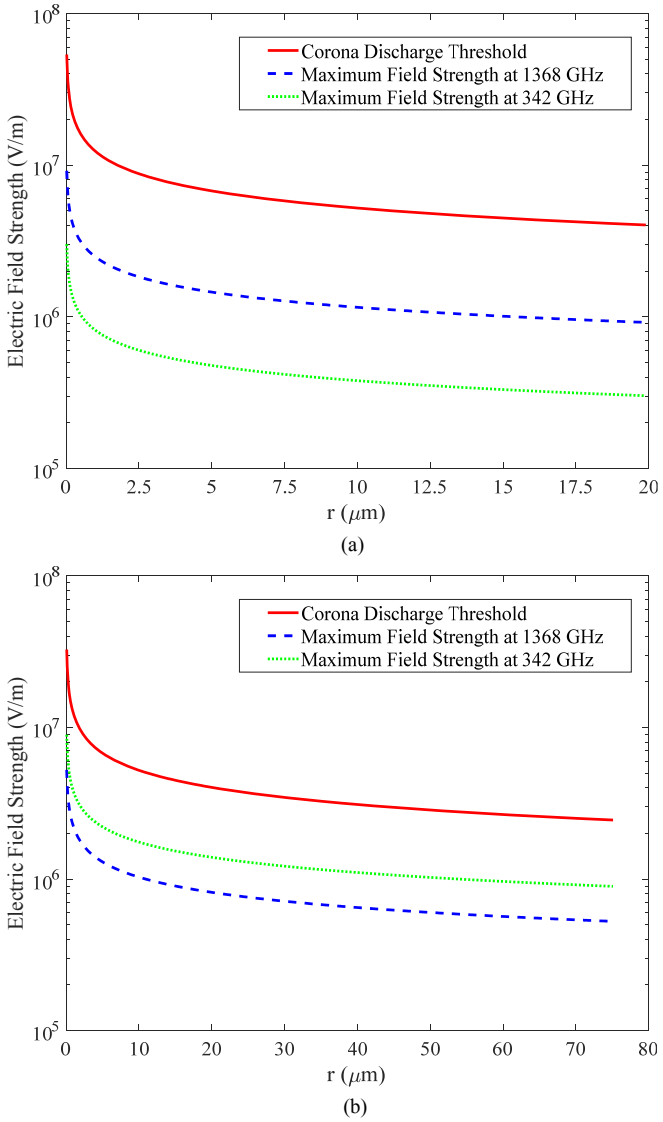

Fig. 7. Variations of the maximum electric field strengths at the designed frequencies and the corona discharge thresholds as functions of r: (a) for the high-pass FSS; (b) for the low-pass one.

IV. THE HIGH-POWER BREAKDOWN ASSESSMENT

As the designed gyro-multiplier is to be operated in short-pulsed mode, the heating of the metal FSSs is negligible. Two types of electric breakdown should be investigated [38]: the volumetric one and the corona one. The corona breakdown [39] should be considered at the vicinity of the 90-degree edges of the circular perforations, where the electrical field singularity occurs. Thus in the following analysis, the volume around a FSS is divided into two sub-volumes: Volume I denotes the one that is within a distance d of the 90-degree edges of the perforations and Volume II encloses the remaining space. d denotes a distance which is small compared to the dimensions of the device. In our case, d is chosen as $L_u/10$, where L_u is shown in Fig. 2. According to [22], the corona discharge and the volumetric breakdown should be considered in Volume I and II, respectively. The maximum electric field amplitude in Volume I can be written as

TABLE IV
MFEF VALUES AT THE DESIGNED FREQUENCIES OF THE TWO FSSS.

	342 GHz	1368 GHz
High-pass, CST	2.01	3.86
High-pass, HFSS	2.00	3.62
Low-pass, CST	3.98	2.21
Low-pass, HFSS	3.88	2.33

$$E_{M1} = E_d * (r/d)^{(\alpha-1)} \tag{2}$$

where r denotes the variable which is the distance to the 90-degree edges of the perforations ($r \leq d$). $\alpha = 2/3$ assuming that the edges are of perfect 90-degree angle. E_d is the maximum electric field amplitude at $r = d$, which can be derived from the aforementioned full wave simulations.

The E_{M1} values and the corona breakdown thresholds for both FSSs are plotted as functions of r in Fig. 7. In Volume I, E_{M1} at the vicinity of the 90-degree edges can assume high values, which however remain lower than the corona breakdown thresholds. It could also be derived that the ratios between the corona breakdown threshold and the E_{M1} values [22] for both FSSs increase as r decreases, implying that the former will remain higher than the later when $r \to 0$. Thus the input power level in our application is unlikely to cause corona breakdown to the designed FSSs.

For the volumetric breakdown issue in Volume II, the maximum electric field E_{M2} induced in the space near the designed FSS should be examined. Since the FSS will be radiated by the two quasi-Gaussian beams simultaneously, E_{M2} can be calculated as

$$E_{M2} = E_{maxLF} + E_{maxHF} \tag{3}$$

where E_{maxLF} and E_{maxHF} are the maximum electric field induced on the FSS by the LF and HF quasi-Gaussian beam incidence, respectively. The electric breakdown problem will occur when

$$E_{M2} > E_{ap} \tag{4}$$

in which E_{ap} is the practical volumetric breakdown threshold of the air at the vicinity of the FSS, considering the surface roughness of the metal plate. E_{ap} can be estimated by [23]

$$E_{ap} = e_R \cdot E_a \tag{5}$$

where $E_a = 3 \times 10^6\ V/m$ is the theoretical volumetric breakdown threshold of air at normal atmospheric pressure. e_R is the roughness factor which characterizes the influence of the surface roughness on the breakdown electric field strength. By taking the aforementioned mean roughness value of 153 nm into consideration, the value of e_R can be estimated as 0.9 [23]. Thus E_{ap} is estimated as $2.7 \times 10^6\ V/m$.

The incident waves on the FSS at 342 and 1368 GHz are quasi-Gaussian beams with the maximum electric field amplitudes of $E_{LF}^{in} = 2.25 \times 10^5$ and $E_{HF}^{in} = 2.38 \times 10^5\ V/m$ [17], respectively. Since the incident waves have non-uniform field distributions, the determination of E_{maxLF} and E_{maxHF} is challenging. However, another set of variables can be defined to estimate their upper limits, which are denoted as E'_{maxLF} and E'_{maxHF}. E'_{maxLF} is the maximum electric field strength induced on the designed FSS when the incident field is a plane wave at 342 GHz with a uniform electric field amplitude of E_{LF}^{in}. E'_{maxHF} denotes the maximum electric field strength on the FSS when the incidence is a plane wave at 1368 GHz with a uniform electric field amplitude of E_{HF}^{in}. It can be interpreted that

$$E_{maxLF} \leq E'_{maxLF} \tag{6a}$$

$$E_{maxHF} \leq E'_{maxHF} \tag{6b}$$

, the equality of which can be assumed when the waist radii of the quasi-Gaussian beams are much larger than the unit cell sizes of the FSSs. The values of E'_{maxLF} and E'_{maxHF} can be calculated by [7]

$$E'_{maxLF} = E_{LF}^{in} \cdot MFEF_{LF} \tag{7a}$$

$$E'_{maxHF} = E_{HF}^{in} \cdot MFEF_{HF.} \tag{7b}$$

The maximum field enhancement factor ($MFEF$) is defined as the ratio between the maximum electric field amplitude at the surface of the FSS and the incident electric field strength, for plane-wave incidence [7]. It has been experimentally verified as an effective parameter for the estimation of the power handling capability of the FSS. Here we define $MFEF_{LF}$ and $MFEF_{HF}$ as the $MFEF$ values at 342 and 1368 GHz, respectively, which can be obtained from the aforementioned full-wave EM simulations. The absence of the electric field singularity in Volume II ensures the convergence in the calculation of the maximum electric field amplitudes and MFEF values with reasonable numbers of mesh cells.

The $MFEF$ values at the frequencies of interests for the high-pass and low-pass FSSs are summarized in TABLE IV. As both numerical tools show similar results at the designed frequencies, the $MFEF$ values from CST MWS will be used in the following discussion. For the high-pass FSS, E'_{maxLF} and E'_{maxHF} can be derived from (7) as 0.45×10^6 and $0.92 \times 10^6\ V/m$, respectively. By combining (3)-(6), it can be derived that for the high-pass FSS,

$$E_{M2} \leq 1.37 \times 10^6\ V/m < E_{ap.} \tag{8}$$

In the same fashion, E'_{maxLF} and E'_{maxHF} can be derived as 0.90×10^6 and $0.53 \times 10^6\ V/m$, respectively, for the low-pass FSS. It can then be obtained that for the low-pass FSS,

$$E_{M2} \leq 1.43 \times 10^6\ V/m < E_{ap.} \tag{9}$$

From the above analysis of the corona discharge in Volume I and volumetric breakdown in Volume II, it can be concluded that both FSSs can operate with the high-power output from the gyro-multiplier.

V. COMPARISON AND DISCUSSION

There are three key factors to be considered when evaluating the FSSs for the high-power THz applications: the transmission and reflection coefficients, the fabrication challenge and the

high-power handling capability.

Firstly, it can be seen from TABLE III that both FSSs are capable of separating the two quasi-Gaussian beams according to the frequencies. The high-pass FSS has better separation performance as the difference between the S_{21} parameters at the two frequencies is larger than that of its low-pass counterpart.

Secondly, the low-pass FSS has approximately four times larger unit-cell sizes than the high-pass one, which can help to significantly alleviate the fabrication difficulties. From Fig. 3 and the microscope measurement, the uniformity of the perforations of the low-pass FSS is better than that of its high-pass counterpart. Besides, the chemical etching or the laser cutting techniques usually require that $H < D$. Due to the increase of the perforation diameter, the thickness of the low-pass FSS can be much larger than its high-pass counterpart. Such feature can help to increase the mechanical strength. When the operating frequencies of the device is further increased to the point where the fabrication of the high-pass FSS is unavailable, the low-pass one is to be used.

The current development status of the fourth-harmonic gyro-multiplier allows the adoption of both FSSs, showing similar power handling capability. For even higher power or frequency operation, the above criteria should be revisited. The FSS configurations also have potential application in other gyro-devices with simultaneous multi-frequency output, such as the double-beam gyrotrons [16] and the gyro-multiplier with corrugated waveguide [24]. Besides, the high-pass FSS can be adopted in the frequency-multiplied Smith-Purcell Free Electron Lasers [40] to filter out the fundamental harmonic wave and facilitate the detection of the second or third harmonic signal. In addition, the low-pass FSS can be used at the output end of the high-harmonic traveling wave tubes [41] to transmit the seventh harmonic wave while attenuating the even higher harmonics content.

VI. CONCLUSION

A comparative study between a high-pass and a low-pass FSS for application in the fourth-harmonic gyro-multiplier output system is carried out. The comparison focuses on the separation performance, the fabrication requirement and the high-power operation capability of the two FSSs. Both FSSs can handle the high-power output from the gyro-multiplier. Compared with the low-pass FSS, the high-pass one has better separation performance but higher fabrication requirement as well as lower mechanical strength. Based on a comprehensive consideration, both FSSs are applicable to the output system of the fourth-harmonic gyro-multiplier output system. The FSS configurations and the analysis in this paper will be useful in other circumstances where simultaneous multi-frequency high-power THz radiation is involved.

ACKNOWLEDGMENT

The authors would like to thank Prof. M. Thumm, Karlsruhe Institute of Technology (KIT), for his suggestions about the electric breakdown assessment. The authors would like to thank X. Cao, Beijing University of Posts and Telecommunications, for his assistance during the fabrication process of the FSS. The authors wish to thank Dr. O. Sushko, Dr. M. Candotti and Dr. M. Torrico, all with Queen Mary University of London, for their suggestions in the measurement of the FSS.

REFERENCES

[1] B. A. Munk, *Frequency Selective Surfaces: Theory and Design*. New York, NY, USA: Wiley, 2005.

[2] L. Botten, M. Cadilhac, G. Derrick, D. Maystre, R. McPhedran, M. Nevière, P. Vincent, and R. Petit, *Electromagnetic Theory of Gratings*, vol. 22. Berlin: Springer, 2013.

[3] G. G. Denisov, S. V. Samsonov, S. V. Mishakin, and A. A. Bogdashov, "Microwave system for feeding and extracting power to and from a gyrotron traveling-wave tube through one window," *IEEE Electron Device Lett.*, vol. 35, no. 7, pp. 789-791, Jul. 2014.

[4] G. Denisov, A. Bogdashov, I. Gachev, S. Mishakin, and S. Samsonov, "New radiation input/output systems for millimeter-wave gyrotron traveling-wave tubes," *Radiophys. Qnantum Electron.*, vol. 58, no. 10, pp. 769-776, 2016.

[5] S. V. Samsonov, A. A. Bogdashov, I. G. Gachev, G. G. Denisov, and S. V. Mishakin, "Proof-of-principle experiment on high-power gyrotron traveling-wave tube with a microwave system for driving and extracting power through one window," *IEEE Microw. Wireless Compon. Lett.*, vol. 26, no. 4, pp. 288-290, Apr. 2016.

[6] M. Li and N. Behdad, "Fluidically tunable frequency selective/phase shifting surfaces for high-power microwave applications," *IEEE Trans. Antennas Propag.*, vol. 60, no. 6, pp. 2748-2759, Jun. 2012.

[7] M. Li and N. Behdad, "Frequency selective surfaces for pulsed high-power microwave applications," *IEEE Trans. Antennas Propag.*, vol. 61, no. 2, pp. 677-687, Feb. 2013.

[8] C.-H. Liu and N. Behdad, "High-power microwave filters and frequency selective surfaces exploiting electromagnetic wave tunneling through ϵ-negative layers," *J. Appl. Phys.*, vol. 113, no. 6, p. 064909, 2013.

[9] C.-H. Liu and N. Behdad, "Investigating the impact of microwave breakdown on the responses of high-power microwave metamaterials," *IEEE Trans. Plasma Sci.*, vol. 41, no. 10, pp. 2992-3000, Oct. 2013.

[10] S. N. Vlasov and I. Orlova, "Quasioptical transformer which transforms the waves in a waveguide having a circular cross section into a highly directional wave beam," *Radiophys. Qnantum Electron.*, vol. 17, no. 1, pp. 115-119, 1974.

[11] G. Denisov, A. Kuftin, V. Malygin, N. Venediktov, D. Vinogradov, and V. Zapevalov, "110 GHz gyrotron with a built-in high-efficiency converter," *Int. J. Electron.*, vol. 72, no. 5-6, pp. 1079-1091, 1992.

[12] J. Jin, M. Thumm, B. Piosczyk, S. Kern, J. Flamm, and T. Rzesnicki, "Novel numerical method for the analysis and synthesis of the fields in highly oversized waveguide mode converters," *IEEE Trans. Microw. Theory Techn.*, vol. 57, no. 7, pp. 1661-1668, Jul. 2009.

[13] D. A. Constable, "The numerical and experimental investigation of gyro-multiplier configurations," Ph.D. dissertation, Dept. Phys., Univ. Strathclyde, Glasgow, Scotland, U.K., 2013.

[14] S. Liu, D. Liu, Y. Yan, S. Yu, and W. Fu, "Theoretical and experimental investigations on the coaxial gyrotron with two electron beams," in *Proc. 40th Int. Conf. Infr., Millim., Terahertz Waves*, Hong Kong, Aug. 2015, pp. 1-2.

[15] X. Li, Y. Alfadhl, X. Chen, W. He, K. Ronald, and A. Cross, "Design of the output system for a gyro-multiplier," in *Proc. 8th UK, Europe, China Millim. Waves THz Technol. Workshop*, Cardiff, United Kingdom, Sep. 2015, pp. 139-140.

[16] D. Liu, W. Wang, T. Song, Q. Zhuang, H. Shen, and S. Deng, "A method to separate radiations from a dual-frequency operation gyrotron," *IEEE Trans. Electron Devices*, vol. 63, no. 5, pp. 2145-2148, May 2016.

[17] X. Li, X. Liu, Y. Alfadhl, K. Ronald, W. He, A. Cross, and X. Chen, "A dual-frequency quasi-optical output system for a THz gyro-multiplier," *IEEE Trans. THz Sci. Technol.*, vol. 6, no. 5, pp. 674-681, Sep. 2016.

[18] C.-C. Chen, "Transmission of microwave through perforated flat plates of finite thickness," *IEEE Trans. Microw. Theory Techn.*, vol. 21, no. 1, pp. 1-6, Jan. 1973.

[19] C. Winnewisser, F. T. Lewen, M. Schall, M. Walther, and H. Helm, "Characterization and application of dichroic filters in the 0.1-3-THz region," *IEEE Trans. Microw. Theory Techn.*, vol. 48, no. 4, pp. 744-749, Apr. 2000.

[20] F. Miyamaru and M. Hangyo, "Finite size effect of transmission property for metal hole arrays in subterahertz region," *Appl. Phys. Lett.,* vol. 84, no. 15, pp. 2742-2744, 2004.
[21] Y. Wang, B. Yang, Y. Tian, R. S. Donnan, and M. J. Lancaster, "Micromachined thick mesh filters for millimeter-wave and terahertz applications," *IEEE Trans. THz Sci. Technol.,* vol. 4, no. 2, pp. 247-253, Mar. 2014.
[22] U. Jordan, D. S. Dorozhkina, V. E. Semenov, T. Olsson, D. Anderson, M. Lisak, J. Puech, I. M. Nefedov, and I. A. Shereshevskii, "Microwave corona breakdown around metal corners and wedges," *IEEE Trans. Plasma Sci.,* vol. 35, no. 3, pp. 542-550, Jun. 2007.
[23] R. Arora and W. Mosch, *High Voltage Insulation Engineering*. New Delhi, India: New Age International, 2008.
[24] I. Bandurkin, V. Bratman, A. Savilov, S. Samsonov, and A. Volkov, "Experimental study of a fourth-harmonic gyromultiplier," *Phys. Plasmas,* vol. 16, no. 7, p. 070701, 2009.
[25] M. Pasian, M. Bozzi, and L. Perregrini, "Accurate modeling of dichroic mirrors in beam-waveguide antennas," *IEEE Trans. Antennas Propag.,* vol. 61, no. 4, pp. 1931-1938, Apr. 2013.
[26] Technology Introduction, ZhongHaiXingRui (Beijing) Technology Co., Beijing, China. (2016). [Online]. Available: http://www.micromesh.com.cn/shike
[27] L. A. Robinson, "Electrical properties of metal-loaded radomes," Reconnaissance Lab., Stanford Res. Inst., Menlo Park, CA, Wright Air Develop. Div. Rep. No. WADD-TR-60-84, Feb. 1960.
[28] CST Studio Suite Help Document, CST Corp., Darmstadt, Germany. (2016). [Online]. Available: http://www.cst.com/
[29] DektakXT Brochure-Bruker, Bruker Corp., Billerica, MA, USA. (2015). [Online]. Available: https://www.bruker.com
[30] HFSS Help Document, ANSYS Inc., Canonsburg, PA, USA. (2015). [Online]. Available: http://www.ansys.com/Products/Electronics/ANSYS-HFSS
[31] M. Kirley and J. H. Booske, "Terahertz conductivity of copper surfaces," *IEEE Trans. THz Sci. Technol.,* vol. 5, no. 6, pp. 1012-1020, Nov. 2015.
[32] X. Shang, M. Ke, Y. Wang, and M. J. Lancaster, "WR-3 band waveguides and filters fabricated using SU8 photoresist micromachining technology," *IEEE Trans. THz Sci. Technol.,* vol. 2, no. 6, pp. 629-637, Nov. 2012.
[33] Selection Guide, Keysight Technologies, Berkshire, United Kindom. (2016). [Online], Available: http://www.keysight.com/en/pcx-x2015001/network-analyzers?nid=-32503.0&cc=GB&lc=eng
[34] A. I. McIntosh, B. Yang, S. M. Goldup, M. Watkinson, and R. S. Donnan, "Terahertz spectroscopy: a powerful new tool for the chemical sciences?," *Chem. Soc. Rev.,* vol. 41, no. 6, pp. 2072-2082, 2012.
[35] C. Winnewisser, F. Lewen, and H. Helm, "Transmission characteristics of dichroic filters measured by THz time-domain spectroscopy," *Appl. Phys. A,* vol. 66, no. 6, pp. 593-598, 1998.
[36] T. Idehara, I. Ogawa, K. Kawahata, H. Iguchi, and K. Matsuoka, "Application of the gyrotron FU II submillimeter wave radiation source to plasma scattering measurements," *Int. J. Infrared Millim. Waves,* vol. 25, no. 11, pp. 1567-1579, 2004.
[37] FEKO User Help Document, Altair Corp., Lincolnshire, IL, USA. (2015). [Online]. Available: https://www.feko.info/
[38] A. D. MacDonald, *Microwave Breakdown in Gases*. New York, NY, USA: Wiley, 1966.
[39] M. Pasian, M. Formaggi, M. Bozzi, F. Carli, L. Perregrini, G. Philippou, and G. Dauron, "Multiphysics design and experimental verification of a quad-band dichroic mirror for deep space ground stations," *IET Microw., Antennas Propag.,* vol. 7, no. 6, pp. 391-398, Apr. 2013.
[40] J. Gardelle, P. Modin, H. P. Bluem, R. H. Jackson, J. D. Jarvis, A. M. Todd, and J. T. Donohue, "A compact THz source: 100/200 GHz operation of a cylindrical Smith–Purcell free-electron laser," *IEEE Trans. THz Sci. Technol.,* vol. 6, no. 3, pp. 497-502, May 2016.
[41] H. Gong, G. Travish, J. Xu, Y. Wei, J. Feng, and Y. Gong, "High-power tunable terahertz radiation by high-order harmonic generation," *IEEE Trans. Electron Devices,* vol. 60, no. 1, pp. 482-486, Jan. 2013.